Magnetic-field study in a compact helical system

H. Yamada, K. Matsuoka, S. Okamura, K. Ida, and K. Nishimura

National Institute for Fusion Science, Nagoya 464-01, Japan

(Received 17 July 1989; accepted for publication 27 September 1989)

Implementation of the designed magnetic field in the compact helical system torsatron device has been verified both experimentally and numerically. A misalignment of the outer two sets of poloidal field coils has been identified both quantitatively and qualitatively. A magnetic-field-mapping experiment has indicated that closed magnetic surfaces have been successfully achieved up to 95% of the outermost surface and that islands exist on the $m = 2$ and 3 major rational surfaces. The experimental results and the computational analysis consistently explain that these islands are mainly caused by the ambient field resulting from magnetization of the building structure. The $m = 2$ island width is estimated to be several millimeters during regular plasma heating experiments when the toroidal field is more than 1 T.

INTRODUCTION

The compact helical system (CHS) torsatron device[1,2] was constructed at the Institute of Plasma Physics, Nagoya University[3] in March 1988. The CHS magnetic configuration has a lower aspect ratio ($A_p \approx 5$) than any other existing helical system: Heliotron-E ($A_p \approx 11$),[4] ATF ($A_p \approx 7$),[5] and Wendelstein VII-AS ($A_p \approx 10$).[6] The CHS project emphasizes studies of transport in currentless low-aspect-ratio toroidal plasmas confined in externally generated helical fields.

While low aspect ratio is favorable from the standpoints of economics[7] and MHD stability,[8,9] it leads to fragility of magnetic flux surfaces due to the enhancement of toroidicity. Since closed magnetic surfaces in CHS are formed by external coil currents similar to those in all stellarator/heliotron/torsatron devices, a strict implementation of the engineering design of the magnetic-coil system is a prerequisite for physics studies. During the construction of the machine, extensive efforts were devoted to suppressing error fields in order to closely realize the designed magnetic field. In particular, the choice of a small cross-section conductor and the use of the vacuum vessel as a frame for the helical-coil windings have led to a highly accurate winding with a winding error of only ± 0.5 mm, adequate tolerance to both electromagnetic and thermal stresses, and small error fields due to crossovers and noncanceling buswork fields.[10–12] These characteristics made it possible to limit individual error fields to $\leqslant 1$ G during operation with a toroidal field $B_t \approx 1$ T. In spite of these precautions, error fields are not necessarily negligible in CHS, as there may be error fields other than those previously indicated. These additional error fields must be identified both qualitatively and quantitatively before the plasma confinement experiments begin.

To verify that the designed magnetic fields have been realized, we carried out a magnetic-field-mapping experiment. We have identified the major causes of significant error fields to be the magnetization of ferromagnetic materials around the machine and the misalignment of the poloidal field coil sets. The magnitude of the various probable error fields is also discussed.

I. CHS COIL CONFIGURATION AND ERROR FIELD CRITERION

The CHS is a torsatron-type device with an $l = 2$ poloidal multipolarity and with eight field periods ($M = 8$). The coil configuration is illustrated in Fig. 1. The major radius of the machine R is 1 m and the minor radius of the helical-field (HF) coil windings is 0.313 m. The designed maximum toroidal field is 2 T, but operation is presently limited to 1.5 T due to limitations of the power supply. In order to achieve a plasma aspect ration $A_p = 5$, a positive pitch modulation of $\alpha^* = 0.3$ was introduced into the HF coil winding law,

$$\theta = (M/l)\phi + \alpha^* \sin[(M/l)\phi], \tag{1}$$

where θ and ϕ are the poloidal and toroidal angles, respectively. The relatively thin hollow conductor was wound into 342 turns (85.5 turns in series and four sets in parallel) inside troughs, which were machined by a numerically controlled lathe, on the vacuum vessel. This achieves a coil winding precision of ± 0.5 mm, resulting in a negligible error field.

The CHS device has four sets of poloidal field coils, each

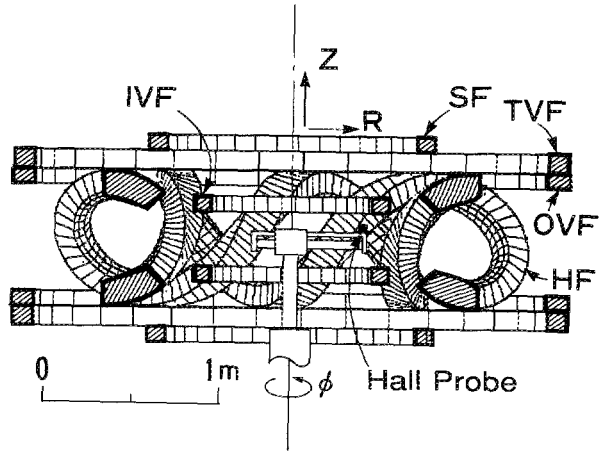

FIG. 1. Coil configuration in the CHS device. A schematic view of the coil misalignment measurement is also shown.

 0034-6748/90/020686-07$02.00

of which has a specific role. The outer vertical field (OVF) coil, with 20 turns, is connected in series with the HF coil and cancels out the vertical field due to the unidirectional HF coil current. The trimming vertical field (TVF) coil, with 33 turns, shifts the flux surfaces in the major radial direction. The OVF and TVF coils are set together in the same supporting frame. The shaping field (SF) coil, with 39 turns, produces a quadrupole field and controls the shape of the flux surfaces and the rotational transform profile. The inner vertical field (IVF) coil, with 60 turns, generates poloidal flux and eliminates the leakage flux around the machine. The last three sets of coils have individually controllable power supplies.

As in Heliotron-E and ATF, CHS has a sheared magnetic configuration with a central rotational transform $\iota(0)$ of around 0.3 and an edge rotational transform $\iota(\bar{a})$ of around unity, where $\bar{a}$ is the average minor radius of the outermost flux surface. Here the rotational transform ι is the number of poloidal turns of the magnetic field line divided by the number of toroidal turns of the line in the limit of an infinite number of toroidal transits. In the CHS magnetic configuration, major low-order rational surfaces such as $m/n = 3/1$, $2/1$, and $3/2$ exist in the plasma-confining region, where m and n are the poloidal and toroidal mode numbers, respectively. Any low-order perturbing fields that resonate with these rational numbers form magnetic islands, thus destroying the simple closed flux surfaces. It is possible to estimate the island width with a simple model, which leads to a criterion for the size of a tolerable perturbation. A rough approximation of the magnetic island width is given by[13]

$$W_{mn} = 4(RB_r^{mn}/mB_t\iota')^{1/2}, \tag{2}$$

where B_r^{mn} is the Fourier component of the perturbing radial magnetic field with a poloidal mode number m and a toroidal mode number n, and $\iota' = d\iota/d\bar{r}$. Here $\bar{r}$ is the average minor radius. In the CHS magnetic configuration, the error field component must be restricted to less than $2.5\times10^{-4}\,B_t$ in order to limit the $m = 2/n = 1$ island width to less than $1/10$ of the plasma minor radius.

It should be noted here that it is dangerous to base a practical design on estimates from a simple Fourier analysis. Careful attention must be paid to the tolerable error field criterion, because the magnetic flux surfaces have a highly complex structure and the toroidal effect is enhanced in CHS because of its low aspect ratio. We have estimated the effect of various probable error fields, which will be discussed in Sec. IV, by using a magnetic-field-line tracing code. The engineering mission was to achieve an accuracy that limits the magnetic field perturbation to $\delta B/B_t \leqslant 1\times10^{-4}$.

II. COIL MISALIGNMENT MEASUREMENT

It has been widely recognized that toroidal plasma confinement devices with rotational transform are sensitive to small coil misalignments.[14,15] This sensitivity is not confined to stellarator/torsatron/heliotron systems but applies to tokamaks as well. Since the winding deviation of the helical coils was held to within ± 0.5 mm in the CHS device, the magnetic surfaces are not destroyed, even if the conductors systematically deform to generate perturbations with low mode numbers. On the other hand, a shift and/or tilt of the poloidal coils can easily induce an effective horizontal, vertical, and/or $m = 2$ perturbation field. Although a uniform vertical perturbation acts only to shift the flux surfaces in the major radial direction, other perturbations can cause magnetic islands and the destruction of flux surfaces. In CHS, the alignment of the OVF and TVF coils is more important, since they have larger magnetic moments and produce larger magnetic fields than the SF and IVF coils. For instance, a shift of 3 mm of both coil sets generates $B_r^{11}/B_t = 5.0\times10^{-5}$, and a tilt of 3 mm induces a perturbation of 1.3×10^{-4} around $\bar{r} = 2\bar{a}/3$. These misalignments are of the order of 0.2% of the dimensions of the coils. We have investigated long scale length deviations of the OVF and TVF coils, as well as misalignments by means of a magnetic field measurement.

A. Experimental procedure

Besides mechanical measurements, a novel technique to experimentally determine coil alignment has been proposed and applied to the URAGAN-3[16] and ATF[17] devices. With this method coil misalignments can be determined by measuring the magnetic fields generated by the poloidal coils.

The OVF and TVF coils were energized by steady-state currents flowing in opposite directions in the upper or lower coils of each set. The coil currents were 6.0 kA/turn for the TVF coils and 9.9 kA/turn for the OVF coils. In this way, a cusp field was formed inside the torus. Deviations in B_R mainly give information about the horizontal displacement of the coils, and deviations of B_Z give information about tilts of the coils. Magnetic fields are measured by a magnetic field sensor (Hall probe) set on the positioning arm. The sensitivity of the magnetic field sensor is 0.01 G. A schematic view of the positioning arm within the CHS coil configuration is shown in Fig. 1. The accuracy of the positioning arm is ± 0.2 mm in the vertical direction and ± 0.1 mm in the radial direction. Deviations of B_R and B_Z were determined by scanning in the R, Z, and ϕ coordinate directions.

B. Experimental results and analysis

Examples of data scans are shown in Figs. 2 and 3. The Hall probe sensor was placed at $R = 0.31$ m and $Z = 0.0$ m. At this position, B_R and B_Z are calculated to be 9.69 and 0 G, respectively. The experimentally observed deviations of B_R are shown as open circles in Fig. 2(a). Since the accuracy of the positioning arm was determined by precise mechanical measurements, the effect of positioning arm misalignment could be calculated numerically. The deviation due to this effect has already been excluded in Figs. 2 and 3. It is clear that an $n = 1$ pattern exists, which suggest a shift of the coils. The dashed line is a computed curve that takes into account coil deformations determined by mechanical measurements. The trends of the observed and computed curves are similar; however, a significant difference can be seen between them. We have separated the source of the deviation into two parts: a horizontal coil shift and an $n = 2$ coil deformation. The latter implies that the coils have a slightly elliptical shape. The solid line is the result of a least-squares fit to

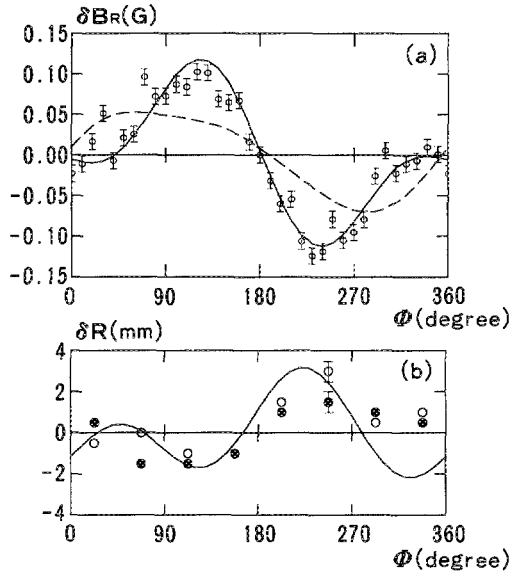

FIG. 2. (a). Toroidal distribution of the radial magnetic field perturbation δB_R at $R = 0.31$ m, $Z = 0.0$ m. The solid line is the result of a least-squares fit to the present model. The dashed line is the δB_R produced by the deformation of the coils, which was obtained by a mechanical measurement. (b) The toroidal distribution of the radial deviation of the coils. The solid line shows the result of the model calculation. The circles represent the deviations obtained from mechanical measurement of the upper (open circles) and lower (solid circles) sets of OVF and TVF coils. The toroidal angle ϕ is defined in Fig. 4.

a number of models that use combinations of these deformations. This line corresponds to a shift of 1.4 mm in the $\phi = 235°$ direction (SW, see Fig. 4 for determination of the direction) and an elliptical deformation of $\pm$ 3.2 mm with the major axis in the $\phi = 45°$ direction.

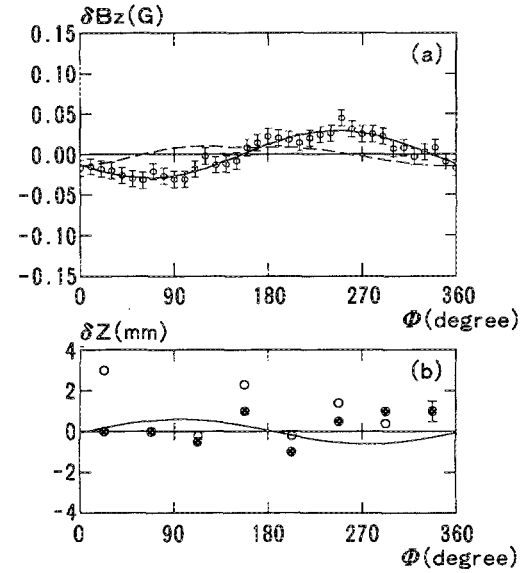

FIG. 3. (a) Toroidal distribution of the vertical magnetic field perturbation δB_Z at $R = 0.31$ m, $Z = 0.0$ m. The solid line is the result of a least-squares fit to the present model. The dashed line is the δB_Z produced by the deformation of the coils, which was obtained by a mechanical measurement. (b) The toroidal distribution of the vertical deviation of the coils. The solid line shows the result of the model calculation. The circles are the deviations obtained from mechanical measurement of the upper (open circles) and lower (solid circles) sets of OVF and TVF coils.

The toroidal distribution of the radial deviation of the TVF and OVF coils is shown in Fig. 2(b). The solid line is the result of fitting to the magnetic field measurements. Circles (open for the upper coil set and closed for the lower coil set) show the results of the mechanical measurements. The tendency of the two measurements is roughly the same. Since the current distribution within a coil cannot be easily ascertained and the center of the current may not coincide with the outer coil surface, the observed discrepancies may be reasonable.

Figure 3 shows the results for the deviation of B_Z, which indicates the vertical displacement of the coil sets. Here, only tilt has been considered. Modeling gives a tilt of $+0.6$ mm in the $\phi = 95°$ direction and -0.6 mm in the $\phi = 275°$ direction.

Field line tracing computations taking into account these error fields indicate that there is no significant destruction of the magnetic flux surfaces but that an $m = 2$ island is formed at $\iota = 1/2$ with a full width of about 6 mm during regular operation.[18]

III. MAGNETIC SURFACE MAPPING

A. Apparatus and experimental procedure

Stellarator/heliotron/torsatron systems have closed vacuum flux surfaces, which are created by external coil currents, unlike the current in a tokamak. This feature enables accurate magnetic field mapping.[19,20]

Figure 4 shows a schematic view of the magnetic-surface-mapping experiment. We employed a fluorescent mesh coated with P15(ZnO:Zn), which has peaks in the fluorescing light at 391 and 504 nm, to project images of the magnetic flux surfaces. The screen was positioned in the most vertically elongated cross section of the magnetic field by being hung from an upper port (see Fig. 5). Unfortunately, the entire screen could not be viewed because of interferences due to the twisted vacuum-vessel wall and the optical

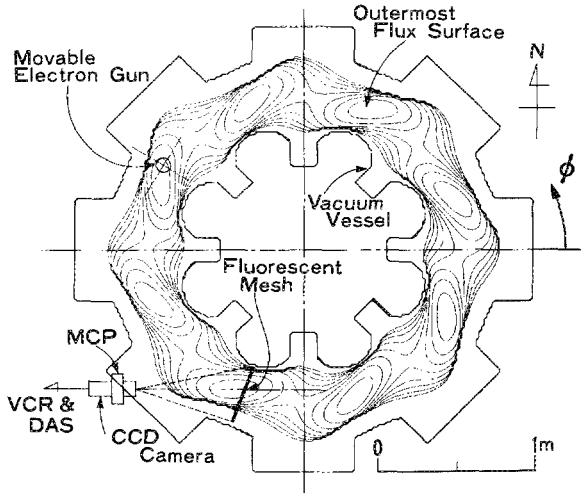

FIG. 4. Arrangement of the magnetic-surface-mapping experiment. Contour plots of a typical outermost flux surface are also shown.

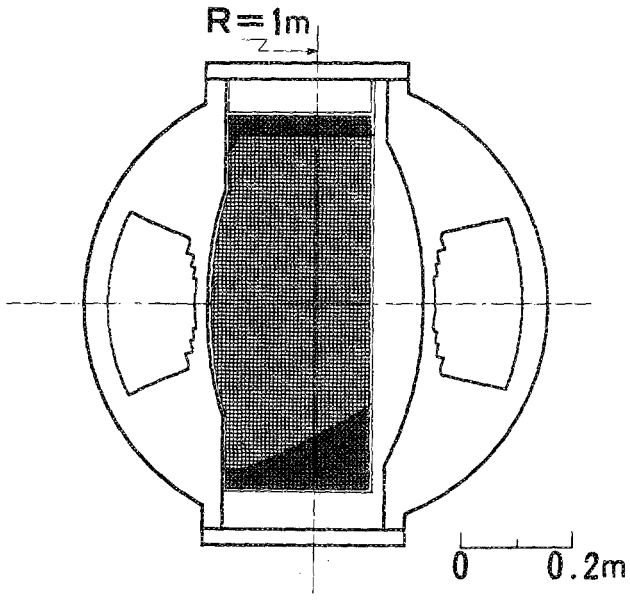

FIG. 5. Cross section of the CHS vacuum vessel showing fluorescent mesh. The shaded region is hidden from view because of the helically twisted inner wall and the viewing angle.

sighting arrangement. The mesh was made of thin (0.1 mm diam) stainless-steel wire, with a grid size of 6×6 mm^2 and an estimated transmittance of approximately 90%. The electron gun, which had an acceleration voltage of 200 V, was located at 100° away from the screen in the toroidal direction and could be moved and swung so as to scan the entire area of the magnetic surfaces. Images from the screen were relayed from a microchannel plate (MCP) through an $f=8$ mm standard video camera lens, which was capable of transmitting wavelengths longer than 350 nm. The maximum radiant emittance gain of the MCP is 10^4 in the range of 400–500 nm. The spatial resolution of the MCP was 27 lines/mm for a modulation transfer function (MTF) = 5%, which corresponds to 3 mm on the fluorescent screen. The phosphor screen behind the MCP was coupled to a 6.6×8.8 mm^2 charged-couple device (CCD) by means of a relay lens. The CCD camera was tuned so as to have a linear response to the measured intensity of the fluorescent light. The outputs of the CCD camera were stored on a video-cassette recorder (VCR) in real time and later transferred through a video digitizer as a 256×256 array to a computer, where the pictures were regenerated and analyzed. Although the experimental resolution was determined by a combination of the mesh size, the resolution of the MCP, and the array size, the most significant factor was the mesh size.

We have conducted magnetic field mapping experiments using steady-state fields up to $B_t = 2.4$ kG. Since only two of the four sets of poloidal field coils (OVF and TVF) could be energized in steady state, magnetic configurations in these experiments were limited. The largest closed surface obtainable was calculated to be $\bar{a}\approx18$ cm, while closed surfaces up to $\bar{a}\approx21$ cm are possible during regular operation. For the maximum toroidal field case, the coil current in one of the two HF coils was 150 kA/turn; currents in the TVF and OVF coils were 25.3 and 35.1 kA/turn, respectively.

B. Experimental results

In the magnetic-field-mapping experiment, our major emphasis was on verification of the existence of the outer closed flux surfaces and on locating magnetic islands. Figure 6 shows the computed magnetic flux surfaces with the largest volume under steady-state experimental conditions. The central rotational transform $\iota(0)$ is 0.27 and the edge rotational transform $\iota(\bar{a})$ is 0.9.

Regenerated images of the magnetic flux surfaces are shown in Fig. 7. Closed magnetic surfaces are observed (except at the major rational surfaces) and, within our experimental resolution, coincide with computed magnetic surfaces. Although the most fragile $\iota=1$ surface does not exist under the present experimental conditions, fine surface structure is observed up to 95% ($\bar{a}\approx17$ cm) of the outermost surface. The outer periphery was not observed because the electron beam tracing the outermost flux surface struck the frame of the secreen at the inner wall. The clearance between the vacuum vessel wall and the outermost surface is small in the CHS because of the pitch modulation term in the winding law.

At major rational surfaces $\iota=1/3$, 1/2, and 2/3, island structures corresponding to rational numbers are observed (see Fig. 8). The fullest width of the $m=2$ island at $\iota=1/2$ is 3 cm when $B_t=440$ G and that of the $m=3$ island at $\iota=2/3$ is 1.5 cm. The $m=3$ island at $\iota=1/3$ is rather small, approximating the level of the experimental resolution. These islands are much larger than predicted by the coil-misalignment study mentioned in Sec. II, while the phase of the islands seems to agree with the predictions within a poloidal angle of 20°. No other islands are detected within the present experimental resolution. The phases of the observed islands are not changed by the reversal of the direction of B_t. The widths of the islands, however, tend to shrink with increasing B_t in the range from 0.4 to 2.4 kG. The magnetic field power dependence of the $m=2$ island size is proportional to $B_t^{-1/2}$ in the range of magnetic field investigated (see Fig. 9).

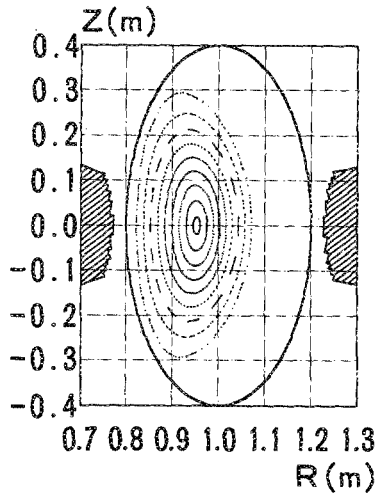

FIG. 6. Computed magnetic flux surfaces for comparison with the magnetic-field-mapping experiments. The outermost magnetic surface has an average radius $\bar{a}$ of approximately 18 cm.

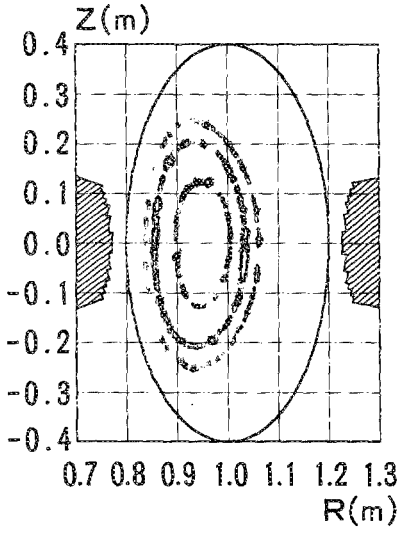

FIG. 7. Experimentally measured images of the magnetic flux surfaces.

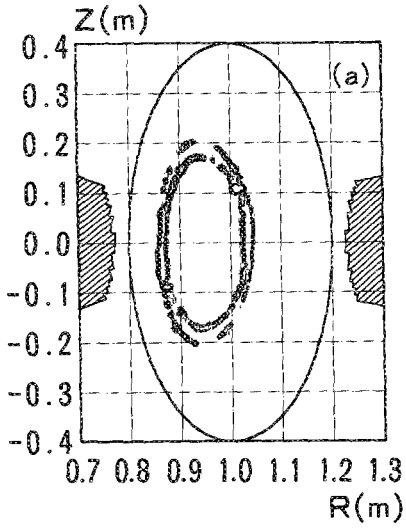

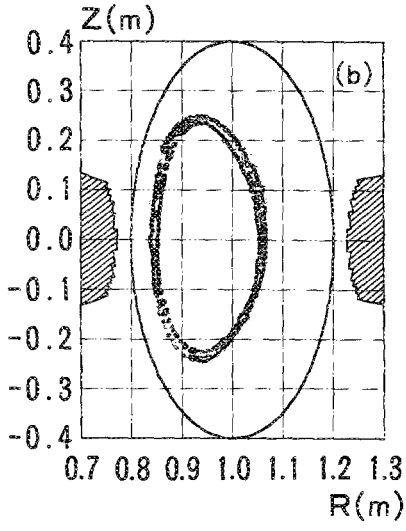

FIG. 8. Experimentally observed images of islands for $B_t = 440$ G. (a) The $m = 2$ island width at the $\iota = 1/2$ surface. (b) The $m = 3$ island at the $\iota = 2/3$ surface.

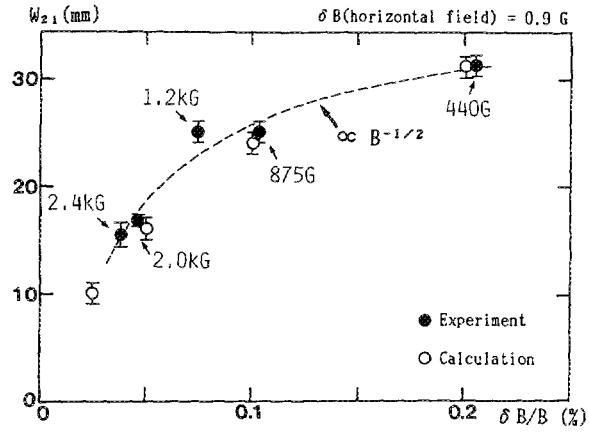

FIG. 9. The $m = 2$ island width at the $\iota = 1/2$ surface as a function of the toroidal magnetic field strength. The closed circles were obtained in the magnetic-field-mapping experiment for various toroidal strengths. The open circles are computed results from a model with a uniform horizontal field perturbation.

C. Perturbations causing magnetic islands

Since the phase of the $m = 2$ island should change by 90° when either B_t or a perturbation field switches its direction, the immutability of the island phase suggests that the direction of perturbation causing a magnetic island changes with the reversal of B_t. We have measured the ambient field around the machine. The ambient field is rather uniform in the NNW direction and points within the range of $85° < \phi < 130°$. Since its strength is about 1.3 G and its angle of elevation is around 45°, the ambient field is approximately decomposed into a horizontal 0.9 G field with a direction of $\phi = 120°$ and an upward 0.9 G vertical field. This ambient field must be due to the magnetization of the building structure, since its strength is considerably larger than the earth's field (about 0.3 G).

Figures 10(a) and 10(b) show islands computed with a horizontal error field of 0.2% of B_t, which may be scaled downward to the experimental values of $B_t = 440$ G and $B_r^{11} = 7.9 \times 10^{-4} B_t$. Model calculations give good agreement with the experiment in both the size and the phase of the islands. Although the vertical component of the perturbation shifts the flux surfaces inward, its level is not detectable in the present experiment. Figure 9 shows the dependence of the $m = 2$ island size on B_t from the model and from the experiment. These observations suggest that while the perturbation causing the island is partially attributable to the CHS machine itself, it is mainly caused by the constant ambient field.

A remaining question is the immutability of the phase of the islands. We have measured the ambient field when the coils were energized in the same manner as in the magnetic-field-mapping experiment. Measurements were made points at $R = 5.0$ m, $Z = 0.0$ m, and $\phi = 90°$ and 270°. On the midplane, the horizontal component of the dipole field produced by the poloidal field coils is zero, and the horizontal field produced by the HF coils is negligible compared with the present ambient field (at most 0.1 G) at $R = 5.0$ m. The direction of the ambient field switches by 180° when the toroidal field is reversed. Its strength remains constant, i. e.,

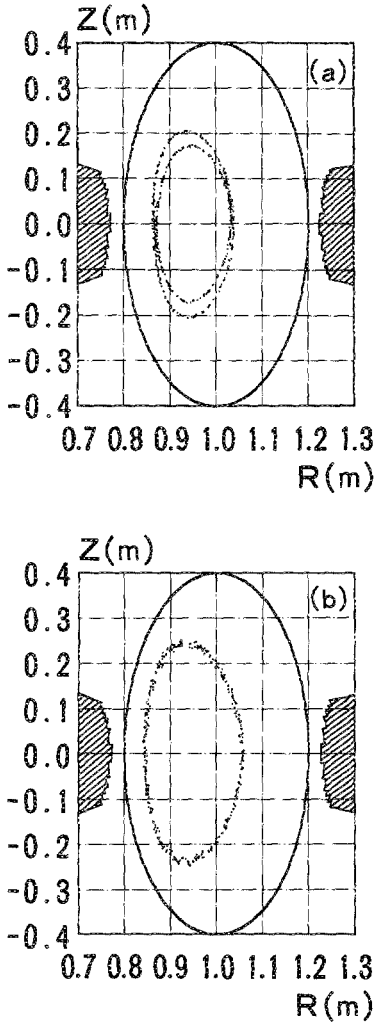

FIG. 10. Computed islands with horizontal error fields of 0.2% of B_t. (a) The $m = 2$ island at the $\iota = 1/2$ surface. (b) The $m = 3$ island at the $\iota = 2/3$ surface.

0.9 G in the range of 240 G $< B_t <$ 1.1 kG. Magnetic field computations show that the stray magnetic field around ferroconcrete structures of the building is typically about 3 G under these conditions, which should saturate the ferromagnetic material.

The experimental results and computational analysis can consistently demonstrate that the error field causing the islands is the ambient field due to magnetization of the building structure by stray flux from the CHS field. Since this field saturates easily, the width of the islands decreases in proportion to $B_t^{-1/2}$. If no other error fields exist, the $m = 2$ island, which is the largest, shrinks to around 6 mm during regular plasma heating experiments at B_t of 1 T. A study of the magnetic flux surfaces with a field line tracing code indicates that both the ambient field and the error field due to the poloidal field coil misalignments can cause $m = 2$ islands of similar phase. Therefore, the actual island is produced by a combination of these two factors. Since the effect of the ambient field is dominant in the range of the toroidal field used during the magnetic-field-mapping experiment, we observed a clear dependence of the island size on the toroidal field. However, the effect of the misalignment of the poloidal field coils becomes more significant with increasing toroidal field, because the error field is directly proportional to the toroidal field. For toroidal fields higher than those investigated in our experiments, the island size is predicted to deviate from the line shown in Fig. 9 as the effect of the other error field, i. e., misalignment of the poloidal field coils, becomes more significant.

IV. DISCUSSION

In this investigation, we have discovered magnetic field perturbations due to the magnetization of ambient ferromagnetic structures and the misalignment of the outer sets of poloidal field coils. Although this gives us a consistent understanding of the experimental observations, many other error fields may be present. The major probable sources of error fields are buswork current feeds and the magnetization of the vacuum vessel. The TVF and OVF coils have nearby current feeds, which generate an asymmetric field perturbation, while the HF coil has four current feeds. The CHS vacuum vessel is made up of eight sectors (four in the toroidal direction, each having an upper and a lower section), which are welded together. Since the material chosen was nitrogen-added stainless steel (SS 304) and electron-beam welding was used, the permeability of the vessel was not significantly changed. Table I summarizes all these error fields and indicates that perturbations other than the two principal error fields discussed are quite negligible. We consider the B_r^{11} field component to be the most dangerous.

Computational analysis involving various probable error fields suggests that no significant destruction of the magnetic flux surfaces is observed in the CHS magnetic configuration. The observed $m = 2$ and 3 islands are caused by the ambient horizontal field and a slight misalignment of the TVF and OVF coils. Although the island widths due to these perturbations are both around 6 mm at $B_t = 1$ T, computational analysis indicates that the island width does not show a simple linear additive response; instead, the island due to the combined factors is smaller. The width of the largest $m = 2$ island is predicted to remain constant at several millimeters for $B_t > 1$ T. Since the shift of the magnetic axis is

TABLE I. Error fields in CHS. The $m/n = 1/1$ Fourier component of the radial field at $\bar{r} = 2/3\bar{a}$ is given.

Error field	B_r^{11}/B_t	Remarks
Ambient field	3.5×10^{-5}	At $B_t = 1$ T 7.9×10^{-4} at $B_t = 440$ G.
Misalignment of OVF and TVF coils	3.6×10^{-5}	Including elliptic deformation.
Buswork of OVF coil	2.0×10^{-6}	
Buswork of TVF coil	1.1×10^{-5}	
Buswork of HF coil	$<10^{-10}$	
Magnetization of poloidal cuts of vacuum vessel	$<10^{-10}$	Even if assume $\mu = 1.1$.
Magnetization of toroidal cuts of vacuum vessel	2.3×10^{-6}	Even if assume $\mu = 1.1$.

controlled by the TVF coils, an inward shift requires larger TVF coil currents, which lead to larger island size.

In the present magnetic-field-mapping experiment, we were unable to obtain information about the $\ell = 1$ surface. The fine structure of the magnetic field in the peripheral regions is of prime importance for plasma-wall interactions and divertor structure. Since natural islands near $\ell = 1$ surface exist in the neighborhood of the outermost magnetic surface, the edge region may be easily perturbed in a macroscopic manner and become ergodic. The magnetic field structure in the periphery, including the region outside the outermost flux surface, will be discussed elsewhere.

ACKNOWLEDGMENTS

The authors thank Dr. R. J. Colchin and Dr. J. H. Harris at ORNL for useful comments and communication.

[1]M. Fujiwara, K. Matsuoka, K. Yamazaki, K. Nishimura, T. Amano, T. Kamimura, H. Sanuki, and J. Todoroki, in *Proceedings of the 12th European Conference on Controlled Fusion and Plasma Physics*, Madrid, 1987, edited by F. Engelmann and J. L. Alvares Rivas (European Physical Society, 1987), Vol. 11D, Part I, p. 4.

[2]K. Matsuoka, S. Kubo, M. Hosokawa, Y. Takita, S. Okamura, N. Noda, H. Yamada, H. Iguchi, K. Masai, S. Morita, K. Ida, H. Idei, C. Takahashi, K. Nishimura, T. Shoji, H. Sanuki, M. Fujiwara, Y. Abe, T. Amano, A. Ando, D.-G. Bi, J. Fujita, S. Hidekuma, T. Kamimura, O. Kaneko, T. Kawamoto, A. Mohri, A. Nishizawa, S. Tanahashi, J. Todoroki, K. Tsuzuki, and K. Yamazaki, in *Proceedings of the 12th International Conference on Plasma Physics and Controlled Nuclear Fusion Research*, Nice, 1988 (International Atomic Energy Agency, Vienna, in press).

[3]The Institute of Plasma Physics, Nagoya University, part of the Plasma Physics Laboratory, Kyoto University, and the Institute for Fusion Theory, Hiroshima University, were united into the National Institute for Fusion Science, the Ministry of Education, Science, and Culture on 29 May 1989.

[4]K. Uo, A. Iiyoshi, T. Obiki, S. Morimoto, M. Wakatani, O. Motojima, A. Sasaki, K. Kondo, M. Sato, K. Hanatani, T. Mutoh, H. Zushi, H. Kaneko, S. Besshou, F. Sano, I. Ohtake, M. Nakasuga, M. Mizuuchi, S. Kinoshita, Y. Nakashima, and N. Nishino, in *Proceedings of the 8th International Conference on Plasma Physics and Controlled Nuclear Fusion Research*, Brussels, 1980 (International Atomic Energy Agency, Vienna, 1981), Vol. I, p. 217.

[5]J. F. Lyon, B. A. Carreras, K. K. Chipley, M. J. Cole, J. H. Harris, T. C. Jernigan, R. L. Johnson, V. E. Lynch, B. E. Nelson, J. A. Rome, J. Sheffield, and P. B. Thompson, Fusion Technol. **10**, 179 (1986).

[6]J. Sapper, U. Brossmann, G. Grieger, J. Kiblinger, S. Mukherjee, F. Rau, B. Sombach, and H. Wobig, in *Proceedings of the 12th Symposium on Fusion Technology*, Julich, 1982 (Pergamon, Oxford, 1982), Vol. 1, p. 161.

[7]J. Sheffield, R. A. Dory, and S. M. Cohn, Fusion Technol. **9**, 199 (1986).

[8]J. F. Lyon, B. A. Carreras, S. L. Painter, J. S. Tolliver, and I. N. Sviatoslavsky, in *Proceedings of the 14th European Conference on Controlled Fusion and Plasma Physics*, Madrid, 1987, edited by F. Engelmann and J. L. Alvares Rivas (European Physical Society, 1987), Vol. 11D, Part 1, p. 353.

[9]B. A. Carreras, N. Dominguez, L. Garcia, V. E. Lynch, J. F. Lyon, J. R. Cary, J. D. Hanson, and A. P. Navarro, Nucl. Fus. **7**, 1195 (1988).

[10]S. Imagawa, Y. Shimanuki, T. Masumoto, Y. Itoh, K. Nishimura, K. Matsuoka, and M. Fujiwara, in *Proceedings of the 15th Symposium on Fusion Technology*, Utrecht, 1988 (North-Holland, Amsterdam, 1989), Vol. 1, p. 412.

[11]K. Nishimura, K. Matsuoka, M. Fujiwara, H. Yamada, S. Okamura, H. Iguchi, M. Hosokawa, K. Ida, S. Imagawa, T. Masumoto, and Y. Itoh, in *Proceedings of the 15th Symposium on Fusion Technology*, Utrecht, 1988 (North-Holland, Amsterdam, 1989), Vol. 1, p. 398.

[12]K. Matsuoka, K. Nishimura, M. Fujiwara, K. Yamazaki, H. Yamada, M. Hosokawa, S. Tanahashi, S. Imagawa, T. Masumoto, and Y. Shimanuki, in *Proceedings of the 12th Symposium on Fusion Engineering*, Monterey, 1987 (Institute of Electrical and Electronics Engineering, New York, 1987), Vol. 2, p. 848.

[13]S. Matsuda and M. Yoshikawa, Jpn. J. Appl. Phys. **14**, 87 (1975).

[14]A. I. Morozov and L. S. Solov'ev, in *Reviews of Plasma Physics* (Consultants Bureau, New York, 1966), Vol. 2.

[15]L. S. Solov'ev and V. D. Shafranov, in *Reviews of Plasma Physics* (Consultants Bureau, New York, 1966), Vol. 5.

[16]R. J. Colchin, J. H. Harris, D. K. Lee, J. A. Rome, S. I. Fedotov, F. I. Ozhere'ev, O. S. Pavlichenko, D. P. Pogozhev, V. M. Zalkind, and J. D. Treffert, Rev. Sci. Instrum. **57**, 1233 (1986).

[17]R. J. Colchin, F. S. B. Anderson, A. C. England, R. F. Gandy, J. H. Harris, M. A. Henderson, D. L. Hillis, R. R. Kindsfather, D. K. Lee, D. M. Million, M. Murakami, G. H. Neilson, M. J. Saltmarsh, and C. M. Simpson, Rev. Sci. Instrum. **60**, 2680 (1989).

[18]In the CHS experiment, "regular operation" refers to the configuration giving the largest volume of the outermost flux surface. This configuration is realized by canceling out 94% of the vertical field and 50% of the quadrupole field generated by the HF coils with the OVF, TVF, SF, and IVF coils. The magnetic axis is around 0.97 m.

[19]G. J. Hartwell, R. F. Gandy, M. A. Henderson, J. D. Hanson, D. G. Swanson, and G. J. Bush, Rev. Sci. Instrum. **59**, 460 (1988).

[20]M. J. Saltmarsh, F. S. B. Anderson, G. L. Bell, J. D. Bell, T. S. Bigelow, M. D. Carter, R. J. Colchin, E. C. Crume, J. L. Dunlap, G. R. Dyer, A. C. England, R. F. Gandy, J. C. Glowienka, R. C. Goldfinger, R. H. Goulding, J. W. Halliwell, J. H. Harris, D. L. Hillis, S. Hiroe, L. D. Horton, H. C. Howe, R. C. Isler, T. C. Jernigan, H. Kaneko, R. R. Kindsfather, R. A. Langley, D. K. Lee, J. F. Lyon, M. Kwon, M. M. Menon, P. K. Mioduszewski, T. Mizuuchi, O. Motojima, M. Murakami, G. H. Neilson, J. Sheffield, J. E. Simpkins, C. E. Thomas, T. Uckan, G. S. Voronov, M. R. Wade, T. L. White, J. B. Wilgen, and W. R. Wing, in *Proceedings of the 12th International Conference on Plasma Physics and Controlled Nuclear Fusion Research*, Nice, 1988 (International Atomic Energy Agency, Vienna, in press).